



Chemical imaging to reveal the resin distribution in impregnation-treated wood at different spatial scales



Michael Altgen^{a,b,*}, Muhammad Awais^a, Daniela Altgen^a, André Klüppel^c, Gerald Koch^d, Mikko Mäkelä^e, Andrea Olbrich^d, Lauri Rautkari^a

^aAalto University, School of Chemical Engineering, Department of Bioproducts and Biosystems, P.O. Box 16300, 00076 Aalto, Finland

^bUniversität Hamburg, Department of Biology, Institute of Wood Science, Leuschnerstraße 91c, 21031 Hamburg, Germany

^cGeorg-August University of Göttingen, Faculty of Forest Science and Forest Ecology, Wood Biology and Wood Products, Büsgenweg 4, 37077 Göttingen, Germany

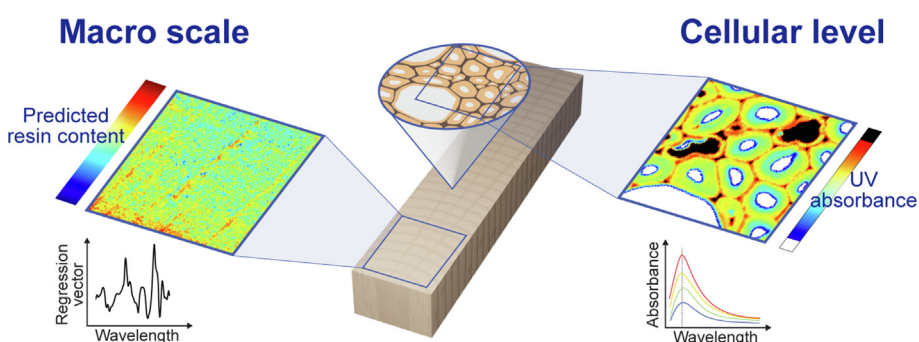
^dThünen Institute of Wood Research, Leuschnerstraße 91c, 21031 Hamburg, Germany

^eVTT Technical Research Centre of Finland, Ltd, PO Box 1000, 02044 VTT Espoo, Finland

HIGHLIGHTS

- Chemical heterogeneity is a common challenge in the application of biomaterials such as wood.
- Chemical imaging methods unravel spatial heterogeneity in wood on different length scales.
- These methods can quantify the chemical distribution in treated wood on macroscopic and cellular levels.
- Combining imaging methods provides a holistic insight into structure–property relations of biomaterials.

GRAPHICAL ABSTRACT



ARTICLE INFO

Article history:

Received 15 April 2022

Revised 6 December 2022

Accepted 7 December 2022

Available online 9 December 2022

Keywords:

Hyperspectral near-infrared (NIR) imaging

Multivariate image analysis

Phenol formaldehyde resin

Ultraviolet (UV) microspectrophotometry

Wood modification

ABSTRACT

An inhomogeneous chemical distribution can be problematic in many biomaterial applications, including wood impregnation. Since wood is a hierarchically structured material, the chemical distribution must be considered on different length scales. Here, a combination of imaging methods revealed the distribution of phenol–formaldehyde resin in impregnation-treated European beech wood within the scale of several millimeters or larger (macroscopic) and the micron scale (cellular level). The macroscopic resin distribution was quantified by hyperspectral near-infrared (NIR) image regression. A partial least square regression model accurately predicted the resin content in the range of 0–30 % with average prediction errors of ≤ 0.93 % for calibration and the test set. The cellular resin distribution was investigated by mapping the UV absorbance in selected regions of interest at high lateral resolution using UV microspectrophotometry (UMSP). The application of both imaging techniques to board sections revealed a process-dependent resin distribution. NIR image regression quantified the drying-induced migration of resin toward the board surfaces. UMSP measurements in selected regions revealed that this resin migration also affected the resin distribution across cell walls. Overall, the results demonstrate the potential of combining chemical imaging techniques to quantify process-dependent heterogeneity and to develop efficient treatments for wood and other biomaterials.

© 2022 The Authors. Published by Elsevier Ltd. This is an open access article under the CC BY license (<http://creativecommons.org/licenses/by/4.0/>).

1. Introduction

Chemical heterogeneity in spatial dimensions is a common problem in the utilization of biomaterials, such as wood. Chemical heterogeneity occurs in native wood, for example, through the dis-

* Corresponding author at: Aalto University, School of Chemical Engineering, Department of Bioproducts and Biosystems, P.O. Box 16300, 00076 Aalto, Finland.

E-mail address: michael.altgen@aalto.fi (M. Altgen).

tribution of heartwood extractives [1–3], but it can also be the result of wood processing and treatment with chemical agents. Besides modern top-down processes that create functional materials from wood scaffolds [4–6], process-dependent chemical distribution is also relevant in traditional impregnation treatments of wood that prevent rapid deterioration in exterior applications [7–10]. Identifying wood regions with insufficient or excessive chemical uptake requires modern chemical imaging techniques to analyze the chemical properties of a sample in spatial dimensions. Applying such imaging techniques to wood is, however, difficult due to its complex hierarchical buildup. Wood appears as a compact solid on the macroscopic scale but consists of long and hollow cells at the microscopic level. For example, fiber cells in hardwoods are typically 0.5–2 mm in length and 10–60 μm in diameter [11]. Therefore, chemical heterogeneity must be considered at the macroscopic level of a wood product on the scale of several millimeters or more, and also across cells at the micron scale.

A prime example of a treatment process that relies on an adequate distribution of a chemical agent in wood at different spatial scales is the impregnation modification with thermosetting resins, such as phenol–formaldehyde (PF) resin. The modification improves the hardness of wood [12] but also protects the wood against fungal decay [13] and dimensional changes caused by water uptake [14]. In impregnation modification, the wood is first impregnated with an aqueous monomer or oligomer solution of PF resin using vacuum and/or pressure. The impregnated wood is then dried, and the resin is heat-cured to form large macromolecules that are irreversibly fixated within the wood structure. The impregnation conditions and the heat-curing step determine the distribution of the resin (or other chemical agents) within the treated wood on the macroscopic and cellular levels [9,10,15–17].

On the micron level, the penetration of the thermosetting resin into the wood cell wall is a prerequisite for sufficient protection. The resin fills space in the cell walls that is otherwise occupied by water, which keeps the wood in a permanently swollen state. This enhances the dimensional stability [9,18] and the resistance of the treated wood against decay fungi [13]. However, the distribution of the resin on the macroscopic level, in the length scale of several millimeters or centimeters, is of equal importance. On this scale, gradients in resin load can result in spatial differences in shrinking and, thus, create stresses, honeycomb splits, and cracks [9,15]. The highly modified surface regions may also not prevent decay in the lesser modified center of a treated board because decay fungi can grow through wood regions with high modification degrees to access other regions in the treated wood [19].

Previous studies on variations in treatment degree across different types of wood often focus on only one spatial scale. For example, the resin distribution across wood cells has been analyzed using chemical imaging techniques with high spatial resolution, such as confocal Raman microscopy [18], confocal laser scanning microscopy [20], or UV microspectrophotometry (UMSP) [13,21]. However, the field of view of these techniques is typically limited to several micrometers, which covers only a small number of wood cells and does not allow for adequately considering heterogeneity on a macroscopic level. Hyperspectral near-infrared (NIR) imaging, on the other hand, enables imaging of larger sample areas with several square centimeters or more, within a period of a few seconds. NIR imaging and multivariate image analyses have been applied successfully to identify different wood species [22] and to map the chemical composition [23], the moisture content [24,25], the distribution of flame-retardant chemicals [26] or the acetylation degree [27,28] in wood. The spatial resolution of hyperspectral NIR imaging does not, however, allow the analysis of wood cells on the micron level and cannot differentiate between chemical agents in cell walls and cell lumens.

Here, two chemical imaging techniques that differ in their lateral resolution and field of view were selected to locate process-dependent heterogeneity in impregnation-modified wood at different spatial scales. NIR image regression quantified the distribution of PF resin in impregnation-modified wood within a several-square-centimeter-large field of view. This was complemented by UMSP measurements on the micron level within selected regions of interest to analyze the resin uptake within individual wood cell types and cell wall layers. The results visualized drying-induced gradients in resin content from the board surfaces to their center on different spatial scales. The outcomes demonstrate the large potential of combining chemical imaging techniques in visualizing process-dependent heterogeneity within wood and other hierarchically structured biomaterials.

2. Materials and methods

2.1. Sample preparation

Two sample sets were prepared from kiln-dried boards of European beech (*Fagus sylvatica* L.) wood. These sets were made of small cubes with edge lengths of 15 mm and board sections with dimensions of $75 \times 15 \times 25 \text{ mm}^3$ (radial, R \times tangential, T \times longitudinal, L). The wood cubes were impregnated to generate a large variation in the PF resin load between different sample groups. These samples served to establish the methodologies to map the resin contents on the macroscopic (hyperspectral NIR imaging) and the micron levels (UMSP). The board sections were treated to generate different gradients in PF resin content within each sample at the same overall resin load. These gradients in resin content were then mapped using the established imaging methodologies.

The small wood blocks were first oven-dried (103 °C for ca. 24 h), cooled in a desiccator over silica gel, and impregnated with aqueous solutions of low molecular weight PF resin (P554; Surfator Germany GmbH) with solid resin contents of 10, 15, 20, 25 or 30 %. Sodium hydroxide was added to improve dilutability with 3 % based on the solid resin content. Reference samples were treated with deionized water without the addition of sodium hydroxide. The samples were first impregnated under vacuum (1 h at 100 mbar) and pressure (2 h at 12 bar), and the excess solution was removed from the surfaces by wiping with a dry cloth. All samples were then heated in sequence at the following temperatures: 20, 40, 60, 80, 40, 103 °C, with each step being held for ca. 24 h. For wet curing, the samples were wrapped in aluminum foil during the first four temperature steps to prevent drying. For dry curing, the samples remained unwrapped and were allowed to dry freely during all curing steps. Five replicates were prepared for each treatment group (separated by solid resin content and curing condition). The board sections were treated in the same way but using only an aqueous PF resin solution with a solid content of 15 %. Furthermore, half of the board sections had their cross-sectional surfaces sealed during the heat-curing stage. The cross-sectional surfaces were covered with aluminum foil, and the board sections were clamped between two wood pieces under gentle pressure. This limited water evaporation from the cross-sectional surfaces during the curing step to create conditions similar to those in commercially sized boards.

In addition to wood samples, a small amount of undiluted stock solution was cured in aluminum cups using the same temperature sequence as with the impregnated wood samples. To simulate wet curing conditions, one aluminum cup with PF resin solution was covered during the first four temperature steps to prevent drying. Another cup with PF resin solution remained uncovered to simulate dry curing conditions.

2.2 Weight and volume changes

The overall resin load of each sample was determined gravimetrically as the weight percent gain (WPG, in %), which is the dry weight added by the treatment related to the initial dry weight of each sample. The WPG was determined again after performing a water-leaching protocol according to EN 84:2020 [29], which involved a vacuum-impregnation (1 h at 100 mbar) of all samples with deionized water followed by water-soaking with regular water changes for two weeks. Volume changes were recorded only for the wood cubes by measuring the edge lengths with a caliper (± 0.01 mm). The wet volume was determined at the end of the water-leaching protocol when the wood cubes were water-saturated. The dry volume was recorded after oven-drying the water-leached samples at ambient conditions for ca. 24 h, followed by oven-drying at 103 °C for another 24 h and cooling in a desiccator over silica gel. Wet and dry volumes were calculated as relative volumes by relating them to the initial dry volume before the treatment.

2.3. Hyperspectral NIR imaging

Before measuring the sample images with the hyperspectral NIR camera, cross-sectional surfaces were prepared by cutting with a circular saw. Excess PF resin that covered the sample surfaces did thus not influence the measurements. Approximately 5 mm slices were removed from one cross section of the small wood cubes, while the board sections were approximately cut in half perpendicular to the fiber direction as illustrated in Fig. 1. Three out of five board sections were further separated into four blocks with a cross-sectional area of ca. 15×15 mm² while the residual two board sections remained in one piece. All samples were stored at the same ambient conditions before hyperspectral NIR imaging.

The cut cross-sectional surfaces were measured with a short-wave infrared (SWIR) spectral camera, which was equipped with an OLES macro lens (both Specim, Spectral Imaging Ltd., Finland) with a focal length of 73.3 mm, a pixel size of ca. 25×25 μm^2 and an image field of view of ca. 10 mm. The speed of the moving stage was adjusted to measure square pixels at an acquisition speed of 30 frames per second. Two rows of halogen lamps generated polychromatic light, and the reflected wavelengths in the range of 935–2550 nm were detected by a HgCdTe detector array

with a grating prism monochromator. The images were collected in line scan mode while the samples moved past the spectral camera. It should be noted that when passing the camera, the width of the samples (ca. 15 mm) exceeded the width of the measured image (ca. 10 mm), hence some areas near the sample edges were not measured. Therefore, the blocks that were cut from the board sections were moved past the spectral camera in different directions compared to the original orientation of the board sections to capture different parts near the radial and tangential surfaces (Fig. 1).

2.4. Multivariate image analysis

Hyperspectral images were measured in reflectance mode, and the raw signal values were preprocessed with a median filter [30]. Principal component analysis (PCA) [31] was used to identify the background, saturated and potentially dead pixels. The remaining pixels were transformed into reflectance using measured spectralon reflectance target and dark current intensities [32]. Regions of interest (ROI) were then selected from the center of each sample image with a size of 451×375 pixels (ca. 11.3×9.4 mm²) for small wood cubes and 2401×375 pixels (ca. 60×9.4 mm²) for the larger board sections. All images were converted into absorbance using Eq. (1)

$$A = \log_{10}(1/r) \quad (1)$$

where r contains unitless reflectance values and A is the estimated absorbance.

Before the quantitative analysis, differences in the test images from the wood cubes were visualized using PCA. For this purpose, an image mosaic was generated by combining individual images from each sample group. The image mosaic was preprocessed with standard normal variate (SNV) [33], mean centered, and the principal component scores and loadings were determined through singular value decomposition [34]. Principal components with high explained variance were considered, and the score vectors were folded back into images.

From the small wood cubes, five replicates per sample group (solid content and curing condition) were scanned, and three images were included in the calibration set and two in the test set. Each image contained 169,125 pixels and the corresponding 288 spectral bands over a range of 935–2550 nm. The bands out-

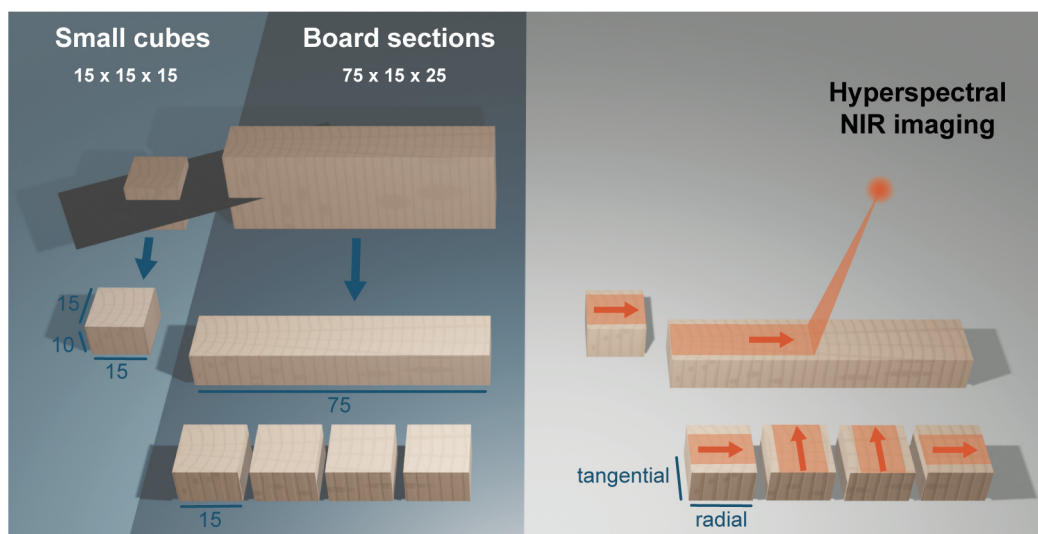


Fig. 1. Sample preparation for the imaging procedure and the directions in which the sample surfaces were scanned with the hyperspectral NIR camera. Note that the camera captured a bandwidth of ca. 10 mm, hence some areas near the edges were not scanned. The image is not to scale.

side the range of 1000–2400 nm were excluded before the analysis because the detector exhibited noise in these bands. Each image was further divided into three sub-sections, and the average spectra per sub-section were collected. The average spectra of all the samples were further divided into calibration and test sets, which contained 102 and 69 objects, respectively. The calibration and test sets were preprocessed with SNV transformation and mean-centered. A calibration model was developed based on the partial least squares (PLS) regression [35] by using the SIMPLS algorithm [36,37] and the gravimetrically determined WPG. The WPG was corrected for the mass loss of ca. 1.5 %, which was caused by the water leaching of native wood extractives. Cross-validation was performed by continuously splitting the training objects into six subgroups, considering similar objects in one group at a time, which left ca. 17 % of objects as a validation set. This method was repeated until all objects had been left out once. Root-mean-squared errors (RMSE) of calibration (RMSEC), cross-validation (RMSECV), and prediction of the test set (RMSEP) were calculated based on Eq. (2):

$$\text{RMSE} = \sqrt{\frac{\sum_{i=1}^n (y_i - \hat{y}_i)^2}{n}} \quad (2)$$

where y_i and \hat{y}_i denoted the measured and predicted values, respectively, and n the number of calibration, cross-validation, or test set objects. The model predicted the WPG in the image mosaic from wood cubes and in images from larger board sections. All data analyses and image processing were performed with in-house Matlab scripts (Matlab R2020b, MathWorks Inc.) and the commercial functions from the PLS toolbox (version 8.7.1, Eigenvector Research Inc.).

2.5. UV microspectrophotometry (UMSP)

The cellular level distribution of the PF resin was analyzed by UMSP, which measured the UV absorbance on thin wood sections in transmission mode. Before the UMSP measurements, small wood pieces with a cross-sectional area of ca. $1 \times 1 \text{ mm}^2$ and a longitudinal length of ca. 5 mm were collected from selected samples and locations using a razor blade. The wood pieces were directly embedded in Spurr's epoxy resin [38] in a mild vacuum with several cycles of evacuation and ventilation, as described by Kleist and Schmitt [39], to avoid chemical modifications caused by reactions with solvents. From the embedded samples, sections with $1 \mu\text{m}$ thickness were prepared on an ultra-microtome with a diamond knife. Each section was transferred to a quartz microscope slide, immersed in glycerin, and covered with a quartz cover slip. The absorbance at a given wavelength (A_λ) was calculated according to Eq. (3):

$$A_\lambda = \log_{10}(I_0/I_x) \quad (3)$$

where I_0 is the intensity of the monochromatic light passing through the embedding resin in the cell lumen, and I_x is the intensity of the monochromatic light passing through a measurement spot of the cell wall layers. The UV/VIS absorbance of cell corners, secondary cell walls, and PF resin deposits in the cell lumens was measured by photometric point measurements with a spot size of $1 \mu\text{m}^2$ in the wavelength range between 240 and 540 nm using a UMSP 80 microspectrophotometer and the LAMWIN® software (both Zeiss, Oberkochen, Germany). Images were taken at a constant wavelength of 278 nm, a lateral resolution of $0.25 \mu\text{m} \times 0.25 \mu\text{m}$, and a photometrical resolution of 4096 greyscale levels using the software APAMOS® (Zeiss, Oberkochen, Germany). False color images of the UV absorbance were prepared using in-house Matlab scripts (Matlab R2020b, MathWorks Inc.). The average UV absorbance at 278 nm was determined from ten representative regions

per sample group within either the secondary cell wall or the cell corner regions.

3. Results and discussion

3.1 Weight and volume changes of small wood cubes

The increase in wood weight and volume caused by the impregnation treatment on the small wood cubes were analyzed, see Fig. 2. The weight changes, determined as WPG, quantified the total PF resin load of each wood cube. The average WPG of each sample group (Fig. 2a) increased with the solid resin content of the impregnation solution independent of the curing conditions, as reported previously [9,18]. A two-week water-leaching protocol caused a small reduction in WPG, possibly due to the removal of unreacted PF resin. However, a small loss in dry weight was also recorded for the reference samples because water leaching removed some wood extractives. The leaching of native wood extractives may have also contributed to the WPG loss of treated wood. After the water-leaching, WPGs up to ca. 30 % were still recorded, which showed that most of the impregnated PF resin was fixated within the treated wood.

In contrast to the weight changes, the changes in volume were not only dependent on the solid content of the impregnation solution but were also affected by the curing conditions (Fig. 2b and c). The wet (water-saturated) wood cube volume remained nearly constant after applying dry curing conditions, while the dry volume increased monotonically with the solid content of the impregnation solution (Fig. 2b). This increase in dry volume showed the incorporation of PF resin within the wood cell wall, where it caused a permanent swelling that is commonly denoted as cell wall bulk-

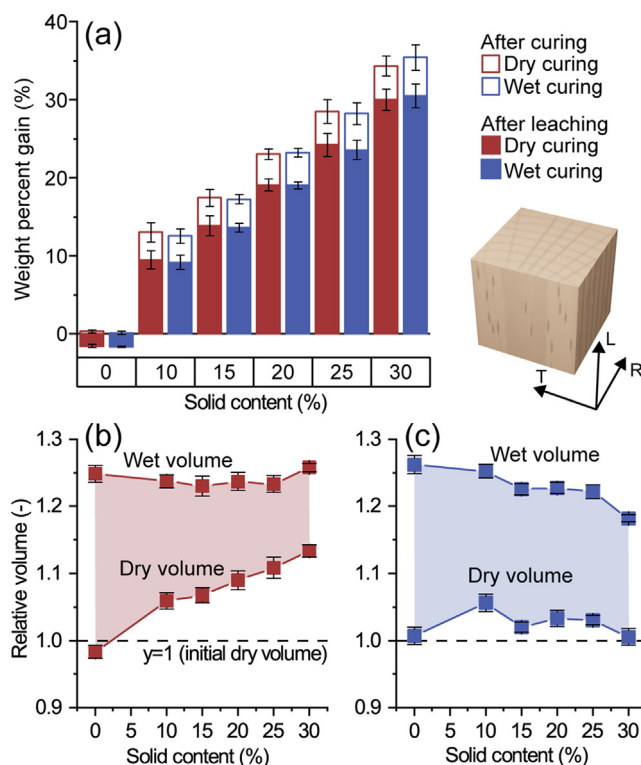


Fig. 2. Changes in weight and volume of small wood cubes: Weight percent gain after heat-curing and after water leaching and its dependence on the solid content of the impregnation solution (a). Changes in relative dry and relative wet volume as functions of the solid content for dry-cured (b) and wet-cured (c) wood cubes. ($n = 5$; \pm standard deviation).

ing. The volumetric margin between the dry and the wet volume was thereby reduced, which increased the dimensional stability of the treated wood. The increase in dry volume was much lower after wet curing and almost negligible after treatment with a 30 % solid content (Fig. 2 c). This lack of cell wall bulking under wet curing conditions has been observed previously and may be explained by alkaline hydrolysis of the cell wall and/or a limited uptake of PF resin by the cell wall [9,18].

3.2. Hyperspectral NIR image analysis and regression

The small wood cubes with a wide range of WPG levels were measured with a hyperspectral NIR camera to study the spatial distribution of WPGs across the wood surfaces. Before the measurements, approximately 5 mm were removed from one cross section with a circular saw to prevent excess resin at the original surface of the wood cubes from affecting the results. Spectra of cured PF resin stock solution were recorded using the same settings as for the wood blocks, but this resulted in a weak signal above ca. 2000 nm for the dry-cured resin (Fig. 3a). Prominent resin bands were still observed, and these band positions coincided with increments in treated wood blocks, particularly within the range between ca. 1600 and 1860 nm and between ca. 2120 and

2220 nm (Fig. 3b). These band regions contain signals from CH groups in aromatic structures, such as phenols [40–43]. The resin treatment also caused small increments in absorbance at ca. 1113 and 2281 nm, with the latter band being assigned to C–H and C–C stretching vibrations in phenols [40]. NIR bands in untreated wood at ca. 1435, 1906–1911, and 2063 nm decreased after the resin treatment. These bands were assigned to water within the wood [44] and indicated a lower moisture content in resin-treated wood.

The effect of the PF resin treatment and differences between the curing conditions were investigated in more detail by PCA, which was performed on an image mosaic of wood cubes treated with different impregnation solutions (0–30 % solid resin content). The first three principal components (PCs) explained 78 % of the variation within the data (Supplementary Fig. S1). The PCA score images and corresponding loadings are shown in Supplementary Fig. S2. The variation explained by the first PC was not directly related to the treatment with PF resin, and high scores were found particularly for pixels around small cracks (wet cured samples with 20 and 25 % solid content) and within some regions of wood cubes treated with a 30 % solid resin content. Higher scores were also found within the latewood regions of the wood cubes compared to earlywood regions and wood rays. The corresponding loading vector showed high loadings for wavelengths below ca. 1380 and above 2220 nm. The first PC was presumably affected by physical aspects of the sample surface rather than by chemical information. In particular, surface roughness, which is a result of the cellular structure of wood or the sample preparation, may have influenced the NIR light reflectance [45].

The second PC showed variation between the different wood blocks related to the PF resin treatment. The corresponding loading vector showed positive bands at ca. 1113, 1659, 2147, and 2281 nm, which could be assigned to phenols [40–43] and corresponded to bands in the NIR spectra of cured PF resin stock solution at the same or similar wavelengths (Fig. 3a). Negative bands in the loading vector at ca. 1441, 1911, and 2063 nm were related to absorbed water in the wood [44]. The increase in scores for treated wood cubes compared to untreated cubes (0 % solid resin content) was thus not only caused by an increased PF resin content but also by the reduction in wood moisture content as an indirect effect of the resin treatment. The smaller increase in scores for wet-cured samples may not imply a lower PF resin content but was presumably related to a lower efficiency of wet-curing conditions to reduce the wood's moisture uptake [46].

The third PC separated wet-cured samples treated with solid resin contents ≥ 20 % from other samples. The negative scores in these wet-cured samples were mostly associated with a negative band in the corresponding loading vector at ca. 2124 nm, which can be assigned to C–H stretching vibrations in the PF resin [40,42,43]. A potential cause for the variation in the third PC could be differences in the chemical structure of the resin related to the curing conditions. An impact of the curing conditions and wood moisture content on the condensation reactions of thermosetting resins within impregnated wood has been observed for wood treatments with partly methylated melamine formaldehyde [18] or melamine urea formaldehyde [47], and similar effects may apply to the PF resin cure.

Since an unsupervised approach based on PCA could not isolate the quantitative differences in PF resin content from other spectral variations, the PF resin distribution was quantified using a PLS regression model. This was based on the average NIR image spectra of the wood cubes and the gravimetrically determined WPG. Based on the average prediction errors of the model calibration (RMSEC) and cross-validation set (RMSECV), four latent variables were chosen to avoid the risk of overfitting (Fig. 4a). The RMSECV reached a minimum at seven latent variables, but the additional decrease in

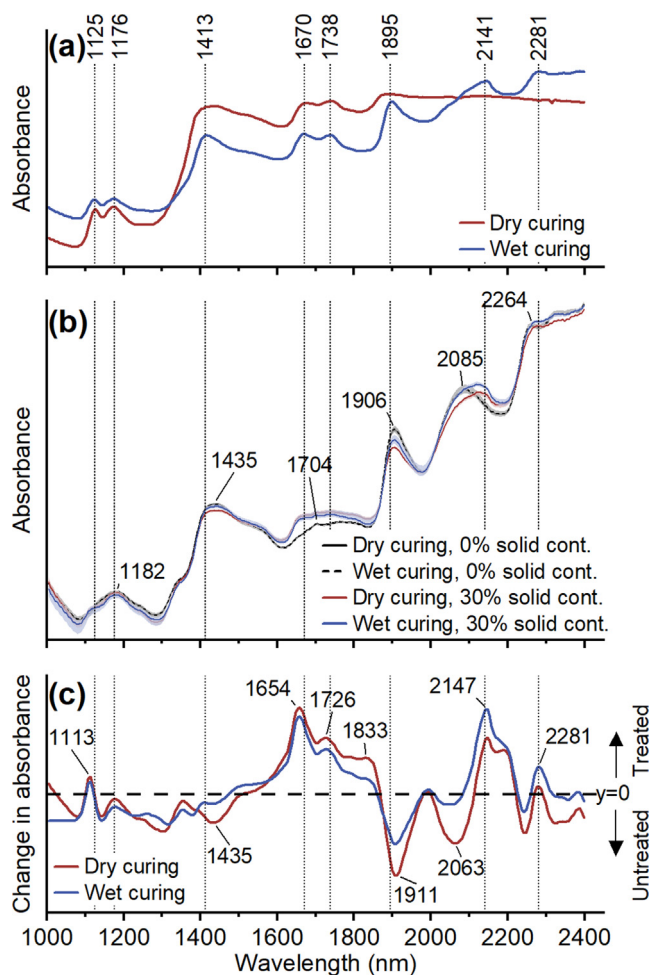


Fig. 3. SNV normalized NIR spectra collected from pure PF resin (a) and from small wood cubes (b) as well as difference spectra between treated (30 % solid content) and untreated (0 % solid content) samples (c). The NIR spectra in (b) are based on the average spectra from the calibration set ($n = 9$), with the lines representing the mean and the shaded areas showing the data range (min/max).

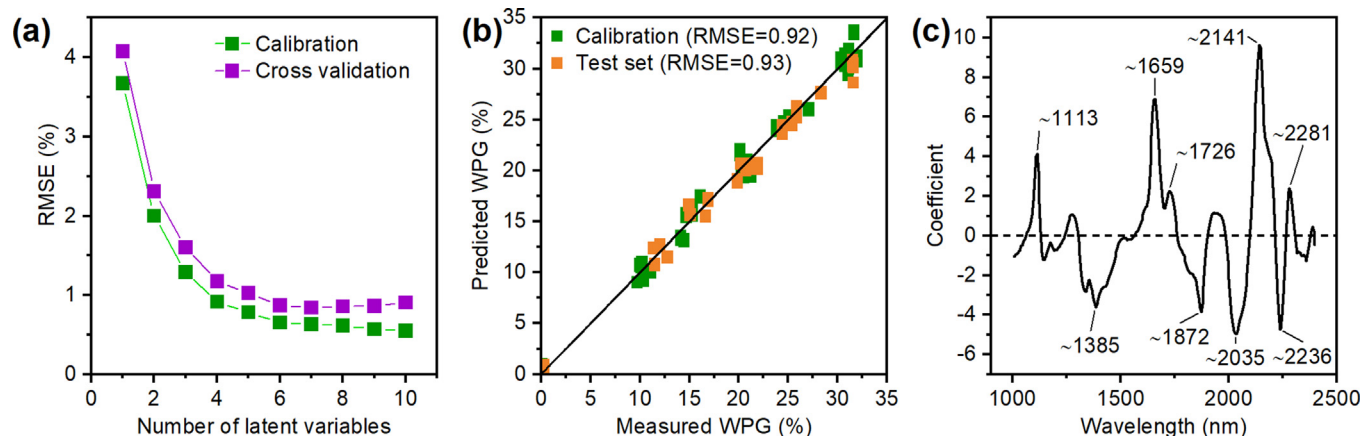


Fig. 4. Results of the PLS regression based on small wood cubes: (a) Calibration and cross-validation errors as a function of the number of latent variables, (b) measured and predicted WPG values of the calibration and test sets based on four latent variables with a solid line showing $y = x$, and (c) the PLS model vector based on four latent variables with the dashed line highlighting $y = 0$.

RMSECV and RMSEC became small when exceeding four latent variables. Four latent variables led to satisfactory predictions of the calibration and test sets (Fig. 4b). Due to the use of wood samples with a wide WPG range, a small underestimation of the test set WPG was only observed at the upper WPG threshold, and the prediction worked particularly well below 30 % WPG. This is important to note given the later application of the calibration model to the board sections with average WPGs below 20 %. The relevant wavelength changes to predict the WPG by the PLS regression model can be seen from the loading vectors of the first four latent variables in Supplementary Fig. S 3 and the model vector in Fig. 4c. In line with the satisfactory WPG prediction, the positive bands in the model vector at ca. 1113, 1659, 2141, and 2281 nm coincided with NIR bands of the cured PF resin stock solution (Fig. 3a). The negative bands in the model vector did not precisely match with the bands at 1441, 1911, and 2063 nm, which were associated with a reduction in the moisture content of the treated wood. However, the influence of wood moisture content variations on the prediction error of the model was not tested. It is thus uncertain if the model can be applied to wood samples that were stored under different climatic conditions before NIR imaging.

The calibration model based on four latent variables was used to predict the WPG on an image mosaic from test set samples that were treated with different impregnation solutions and curing conditions (Fig. 5a). The results show a distinct sample-to-sample variation in WPG in line with the gravimetrically measured WPG. The predicted WPG increased with the solid resin content of the impregnation solution, independent of the curing conditions. The average predicted WPG for each image was close to the measured WPG, with a maximum deviation of 1.4 % points (Fig. 5b). The only exception was the dry-cured sample treated at 30 % solid resin content, for which the average WPG was overestimated by ca. 2.6 % points. This was presumably related to the larger prediction error of the calibration model at high WPG.

There was little variation in predicted WPG within the individual samples (Fig. 5a), and the pixel predictions formed a unimodal distribution over the WPG range of each sample (Fig. 5b). We did not observe notable WPG gradients from the center of the samples toward the edges. However, bands with slightly different WPG levels stretched horizontally in the tangential direction, which corresponded to the earlywood and latewood regions. Earlywood cells have larger cell lumens and thinner cell walls than latewood cells, and more resin likely entered the more porous earlywood regions during the impregnation step. Furthermore, the dry-cured samples with 30 % solid resin content showed radial lines in the vertical

direction with lower WPG, which corresponded to the broad rays in European beech.

3.3. UMSP imaging on small wood cubes

The presence of PF resin in cell walls and cell lumens was topochemically analyzed by UMSP at high spatial resolution using thin sections prepared from the center of the small wood blocks. The UMSP technique measured the UV absorbance of individual cell types and cell wall layers in transmission mode. First, the absorbance was determined over a broad wavelength range in selected regions of the beech wood tissue (Fig. 6). The UV spectra of lumen deposits with cured PF resin showed a distinct absorbance at 280–282 nm and a small shoulder band at around 350 nm (Fig. 6a). There were no obvious differences in the absorbance spectra of the PF resin depending on the curing conditions. The deposition of PF resin in the cell corners (Fig. 6b) and secondary cell walls of fibers (Fig. 6c) significantly increased the natural UV absorbance of beech tissue. Untreated beech showed a characteristic absorbance maximum at 276–280 nm due to the presence of lignin as a native wood constituent [48]. The natural variation in lignin concentration led to a higher UV absorbance in the cell corners and compound middle lamella than in the secondary cell wall. Treatments with PF resin enhanced this natural UV absorbance at both locations.

Since the thickness of the sections was constant, the increase in absorbance after the treatment could be assigned to the increment of PF resin concentration following the Beer-Lambert law. However, the absorbance maximum slightly varied between treated and untreated wood and even between different morphological regions in untreated wood. In line with Musha and Goring [49], the absorbance maximum in untreated wood shifted from 276 nm in the fiber cell walls to 280 nm in the cell corners, presumably due to differences in the syringyl/guaiacyl ratio within the lignin. In the fiber cell walls, the PF resin treatment caused a similar shift in the absorbance maximum from 276 to 280 nm. This was in line with the absorbance maximum at 280–282 nm for the cured PF resin from the cell lumens.

The UV absorbance across beech wood cells was mapped at high lateral resolution at a wavelength of 278 nm. This wavelength has been used previously in UMSP imaging of European beech wood to localize lignin [48] and PF resin [13]. The image profiles showed detailed variations in UV absorbance due to the natural distribution of lignin and the uptake of PF resin. Fig. 7 shows representative UMSP images and pixel histograms based on samples treated

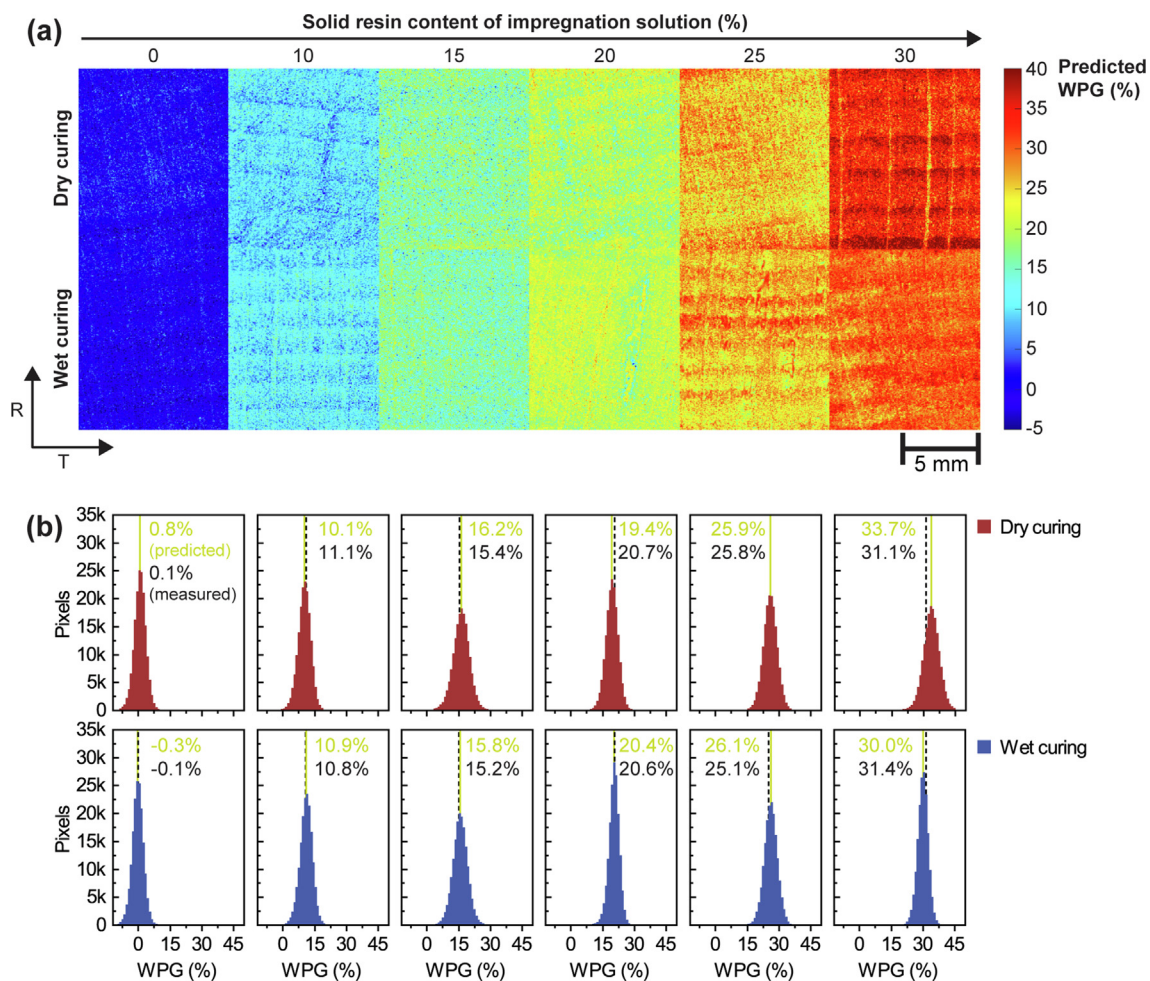


Fig. 5. Predicted WPG values for an image mosaic based on wood cubes treated with different impregnation solutions and curing conditions (a), and the corresponding pixel histograms (b). The arrows in (a) highlight the anatomical directions of the wood (radial and tangential). The vertical lines in (b) show the measured (dashed lines) and the predicted (solid lines) average WPG per NIR image.

with 0 (reference), 15, and 30% solid resin content. Further images taken from the same samples are illustrated in [Supplementary Fig. S4](#). The variation in UV absorbance followed the natural cellular lignin distribution in untreated wood and was higher within the compound middle lamella and the cell corners (average absorbance 0.48) and lower within the secondary cell walls (average absorbance 0.13).

The PF resin treatment led to an increase in UV absorbance across the entire cell tissue, which was dependent on the curing conditions. A two-sample *t*-test for unpaired data based on all pixels per sample group determined significant differences ($p < 0.01$) in UV absorbance between dry- and wet-cured samples ([Supplementary Table S1](#)). In detail, the pixel histograms in [Fig. 7](#) show a shift toward a higher UV absorbance caused by the resin treatment and also indicate the impact of the curing conditions. At 15% solid resin content, differences between the curing conditions were small and only noticeable by a higher proportion of pixels within the absorbance range of 0.3–0.5 in dry-cured wood. At 30% solid resin content, the effect of the curing conditions became more obvious as most pixels were distributed around two distinct peaks in wet and dry cured wood at bin centers of 0.375 and 0.675, respectively. Natural variations of the UV absorbance within the lignocellulosic matrix depending on the anatomical structures were considered by measuring at least five representative image profiles, each containing over 20,000 UV signals (measuring points $0.25 \mu\text{m} \times 0.25 \mu\text{m}$).

The average UV absorbance of the secondary cell walls was determined from selected areas within the UMSP images ($n = 10$), and these average values coincided with peaks in the corresponding histograms ([Fig. 7](#)). The resin treatments resulted in a continuous increase in UV absorbance within the secondary cell wall, which reached an average of 0.26 and 0.38 for wet-cured samples and an average of 0.35 and 0.62 for dry-cured samples after treatments with 15 and 30% solid resin contents, respectively. A difference between the curing conditions was less obvious in the cell corners, where an average absorbance of 1.1 was reached for dry- and wet-cured samples treated with a 30% solid resin content. The stronger increase in UV absorbance within the secondary cell walls after dry curing was consistent with the cell wall bulking effect that was observed as an increase in dry wood volume. A facile diffusion of the PF resin into the cell walls under dry curing conditions may have been favored by the rapid removal of the solvent (water) from the impregnated wood, which increased the solute (resin) concentration in the cell lumen. The concentration gradient between the cell lumen and cell wall thus became larger and was the main driving force for diffusion [9].

The lower increase in UV absorbance of wet-cured samples coincided with their lower cell wall bulking compared to dry-cured samples. Heating the samples without drying may have been unfavorable for the diffusion of the resin into the cell walls because major quantities of PF resin formed macromolecules that were too large to enter the cell wall before the removal of the solvent

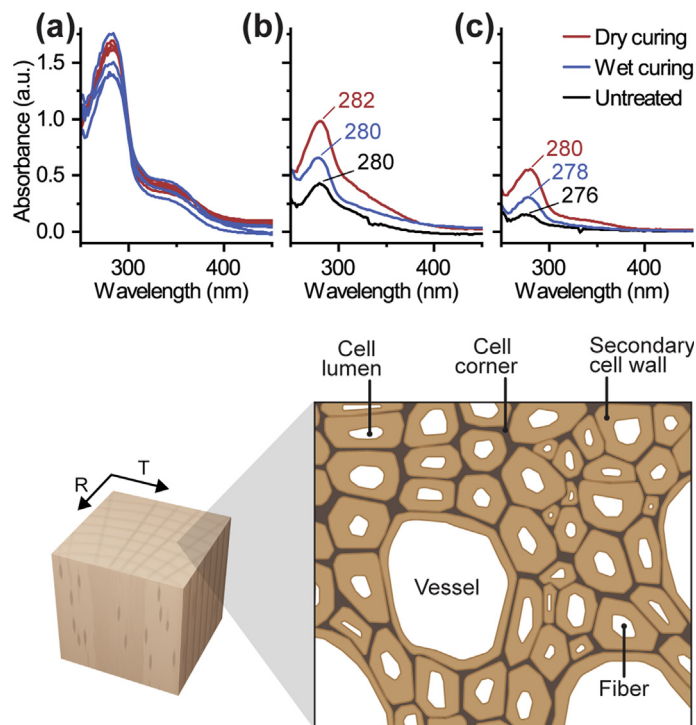


Fig. 6. UV absorbance spectra in the wavelength range between 250 and 450 nm measured from (a) PF resin deposits in the cell lumens, (b) the cell corners, and (c) the secondary cell wall (S2 layer). The measurements were performed on an unmodified cube and cubes treated with 30 % solid resin content. The illustration at the bottom shows the locations within the wood tissue at which the absorbance spectra were measured.

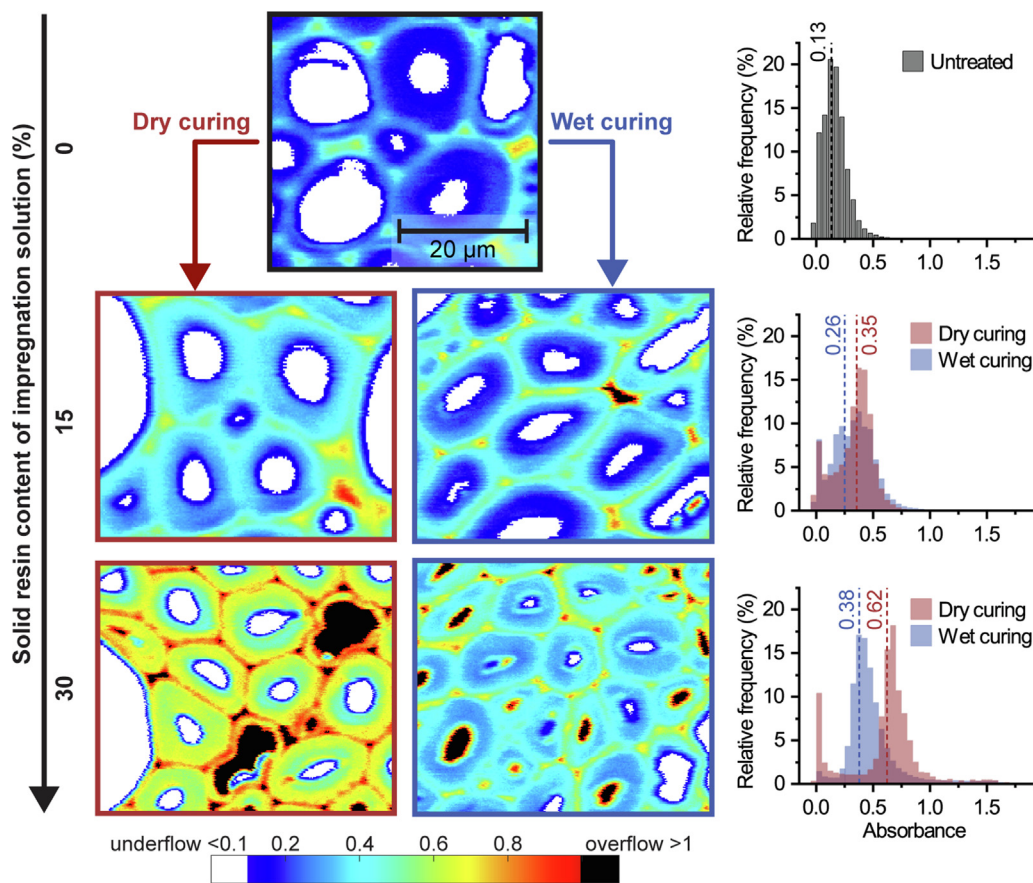


Fig. 7. Representative UMSP image profiles based on the absorbance at 278 nm and pixel histograms from all measured UMSP image profiles per sample group. The dashed lines in the histograms show the average absorbance measured from ten selected regions within secondary cell walls.

increased the concentration gradient [9]. Furthermore, sodium hydroxide was added to the impregnation solution with 3 % based on the solid resin content. Sodium hydroxide can catalyze the dissolution of lignin [50]. Although the sodium hydroxide concentration in the solution did not exceed 0.9 mass-%, it is possible that this had a small effect on the UV absorbance. It may be speculated that the lignin dissolution was stronger under wet curing conditions thus causing a lower UV absorbance. The lack of cell wall bulking under wet-curing conditions may have been a combination of limited diffusion of PF resin into the cell walls [9] and alkaline hydrolysis of the cell wall that counterbalanced the effect of the resin uptake [18].

The UMSP image profiles in Fig. 7 and Supplementary Fig. S3 also show the deposition of cured PF resin within the cell lumens, particularly in wood treated with 30 % solid resin content. In previous studies, such lumen deposits were observed more frequently when wood was treated with larger-sized PF resin oligomers, which were less effective in penetrating the wood cell wall [13,14]. A similar effect may have been expected for wet-cured wood, but the presence and frequency of such lumen deposits could not be related to differences in curing conditions. Presumably, the UMSP images did not represent the number of resin deposits within the cell lumens adequately, since they covered only a small proportion of the cells within the treated wood. Furthermore, wood cells containing resin deposits in their lumen did not show a higher UV absorbance of their cell walls, except for the narrow cell wall regions at the very interface to these lumen deposits.

3.4. Process-related PF resin distribution across board sections

In contrast to the small wood cubes, the board sections were all impregnated using a PF resin solution with a 15 % solid content but were dried and heat-cured in different conditions. While this resulted in the same overall WPG (see Supplementary Fig. S5), it was expected that the variation of the curing conditions would have a significant effect on the distribution of the PF resin within the board sections. The aim was to quantify this distribution first on the macroscopic scale by applying our PLS regression model to the NIR images taken from cross-sectional surfaces, and then on the micron scale using UMSP imaging within selected regions of interest.

Fig. 8 shows the predicted WPG distribution of images that were taken from board sections after cutting them in half, perpendicular to the fiber direction. Further images from replicates are shown in Supplementary Fig. S6. The line averages in Fig. 8 also highlight changes in predicted WPG in the tangential direction (Fig. 8). These were calculated by averaging the predicted WPG in each row based on images from the middle parts of the board sections ($n = 6$). The predicted WPG distribution across board sections was found to be dependent on the conditions during the curing step and the sealing of the outer cross sections. When the cross sections were sealed during the heat-curing step (Fig. 8a), an increase in predicted WPG was observed from the center toward the surface regions of the board sections. The line averages in Fig. 8 show that the predicted WPG increased in the tangential direction from about 17 % at the center to 20 % and more near the surfaces. A more gradual WPG increase was observed for wet-cured board sections, whereas dry curing resulted in a sharp WPG increase and a larger difference in WPG between center and surface regions.

By sealing the cross sections, evaporation of water occurred only at the radial and tangential surfaces. As studied extensively for the technical drying of timber, this evaporation is the driving force for the capillary flow of water through the porous wood structure toward the surfaces [51]. The capillary flow also trans-

ported the dissolved, low molecular weight PF resin toward the surface regions where the resin was eventually heat cured to immobile macromolecules [9]. NIR image regression quantified this resin migration, although some regions near the surface could not be measured. The results showed a stronger migration of resin toward the radial and tangential surfaces after dry-curing compared to wet-curing conditions. Under wet-curing conditions, drying the impregnated wood was limited during the initial increase in temperature. Significant proportions of the resin may thus have been cured to immobile macromolecules before wood drying was initiated at a later curing stage [9].

There was almost no gradient in the predicted WPG from the center to the surface regions when the cross-sections remained unsealed during the heat-curing step (Fig. 8b). Without sealing, the water also evaporated from the cross-sectional surfaces, which initiated the capillary flow of the solution in the longitudinal direction in addition to the flow in the lateral direction. The water transport through the mostly longitudinally oriented cells in wood is much faster than the water transport in the lateral (radial or tangential) directions [52,53]. Thereby, the drying of impregnated, unsealed board sections caused the PF resin migration mostly in the longitudinal direction. This can be seen in the NIR images of unsealed, dry-cured samples by the lower predicted WPG across the cross-section from the central plane of the board sections. In contrast, the limitation of drying during the first temperature steps under wet curing conditions prevented such strong translocation of PF resin in the longitudinal direction and resulted in much higher predicted WPGs in the corresponding NIR images. The line averages in Fig. 8 further highlighted the almost constant WPGs on cross-sectional surfaces in the tangential direction, which remained at about 15 and 18 % in dry- and wet-cured board sections, respectively.

NIR image regression also revealed lower predicted WPGs within the rays in beech wood, which stretch over the cross-sectional surface in the radial direction. This was observed for most sample groups, except for dry-cured board sections without surface sealing. Rays in beech wood are possible transport pathways for the PF resin solution in the radial direction, either during the vacuum-pressure impregnation or during heat curing. However, the treatment of small wood cubes did not result in notably larger WPGs of wood rays (Fig. 5a). Due to their smaller size, the transport of PF resin within the small wood cubes may have been dominated by the rapid transport in the longitudinal direction, and radial transport became only relevant in the larger board sections.

While the NIR image regression successfully quantified the process-dependent distribution of PF resin on the macroscopic level, it did not allow a differentiation between PF resin in the cell lumens and the cell walls. This was achieved by utilizing the high spatial resolution of the UMSP technique to analyze the cellular level distribution of the PF resin in selected regions of interest, near the surface and at the center of the board sections with sealed cross sections (Fig. 9). A two-sample *t*-test for unpaired data based on all pixels per sample group determined significant differences ($p < 0.01$) in UV absorbance between surface and center regions for dry- and wet-cured samples (Supplementary Table S2). In detail, this was observed by a shift to higher absorbance values in the pixel histograms. In line with the peaks in the pixel histograms, the average cell wall absorbance increased from 0.35 at the center to 0.44 and 0.49 at the surface of wet- and dry-cured board sections, respectively. There was also a difference between the two regions in the average UV absorbance of the cell corners, which increased from 0.98 and 0.99 at the center to 1.12 and 1.08 near the surfaces of wet- and dry-cured samples, respectively. Thereby, UMSP confirmed the results of the NIR image regression and also showed that higher predicted WPGs toward the board surfaces were not just due to the deposition of PF resin within

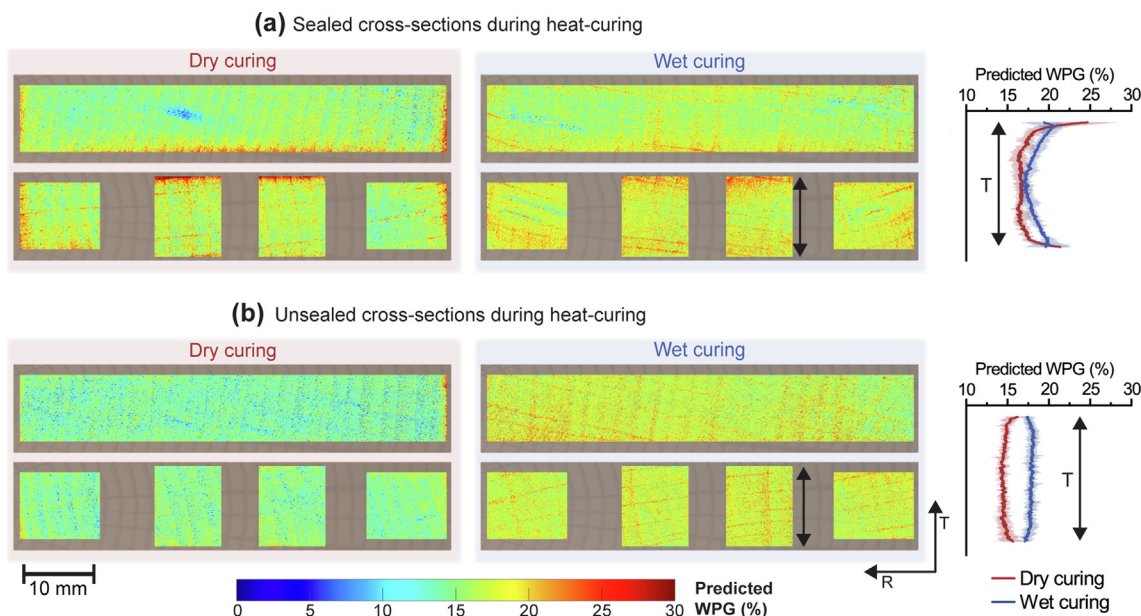


Fig. 8. Predicted weight percent gain (WPG, %) of images from treated board sections. (a) Board sections with sealed cross-sectional surfaces during heat curing; (b) board sections with unsealed cross-sectional surfaces during heat curing. The line plots show the line averages of the predicted WPG in the tangential direction based on samples from the middle of the board sections ($n = 6$; mean \pm min/max). The arrows highlight the anatomical directions of the wood (R radial, T tangential). The placement of the images on the board sections serves as a guide to the eye.

the cell lumen but correlated with higher PF resin content of the wood cell walls. Such differences in PF resin content of cell walls within different board regions lead to strong cell wall bulking near the board surfaces, while the center regions may shrink to a considerable extent upon drying. This favors the formation of inner cracks and honeycomb splits [9,15], and board regions with insufficient PF resin content in the cell walls may also remain susceptible to fungal decay [13]. The chemical imaging approach presented in this study may support generating more homogeneous resin distributions at the macroscopic scale and the cellular level to prevent this and paves the way for the development of more efficient treatments for wood and other biomaterials.

4. Conclusions

This study shows the big potential of combining different chemical imaging methods to unravel process-dependent heterogeneity in hierarchically structured biomaterials. This was demonstrated for an impregnation treatment of wood with PF resin. A NIR image regression model was established based on small wood cubes with a large range of gravimetrically determined PF resin contents. The application of this model to larger board sections revealed the macroscopic distribution of the PF resin across the wood and its significant dependence on the applied heat-curing conditions. The NIR image regression approach was complemented by cellular UMSP imaging within a limited field of view but at a high spatial resolution. This revealed the dependence of the PF resin content of cell walls on the applied curing conditions and the location within board sections. Higher resin contents were found in the cell walls of dry-cured samples and cell walls close to the board surfaces.

Funding

This research did not receive any specific grant from funding agencies in the public, commercial, or not-for-profit sectors.

Data availability

The raw data required to reproduce these findings are available to download from [<https://doi.org/10.5281/zenodo.7304357>] and [<https://doi.org/10.5281/zenodo.7307383>].

[dataset] M. Altgen, M. Awais, D. Altgen, A. Klüppel, G. Koch, M. Mäkelä, A. Olbrich, L. Rautkari, Chemical imaging data collected on small wood cubes after impregnation-treatment with phenol formaldehyde resin, Zenodo, 2022, <https://doi.org/10.5281/zenodo.7304357>.

[dataset] M. Altgen, M. Awais, D. Altgen, A. Klüppel, G. Koch, M. Mäkelä, A. Olbrich, L. Rautkari, Chemical imaging data collected on wood board sections after impregnation-treatment with phenol formaldehyde resin, Zenodo, 2022, <https://doi.org/10.5281/zenodo.7307383>.

CRediT authorship contribution statement

Michael Altgen: Conceptualization, Investigation, Supervision, Visualization, Writing – original draft. **Muhammad Awais:** Formal analysis, Investigation, Methodology, Software, Writing – review & editing. **Daniela Altgen:** Conceptualization, Investigation, Visualization. **André Klüppel:** Investigation, Writing – review & editing. **Gerald Koch:** Resources, Writing – review & editing. **Mikko Mäkelä:** Resources, Supervision, Writing – review & editing. **Andrea Olbrich:** Investigation, Writing – review & editing. **Lauri Rautkari:** Resources, Supervision.

Declaration of Competing Interest

The authors declare that they have no known competing financial interests or personal relationships that could have appeared to influence the work reported in this paper.

Acknowledgements

We thank Tanja Potsch, Daniela Paul, and Gabriele Ehmke for their help with the UMSP measurements. This work made use of

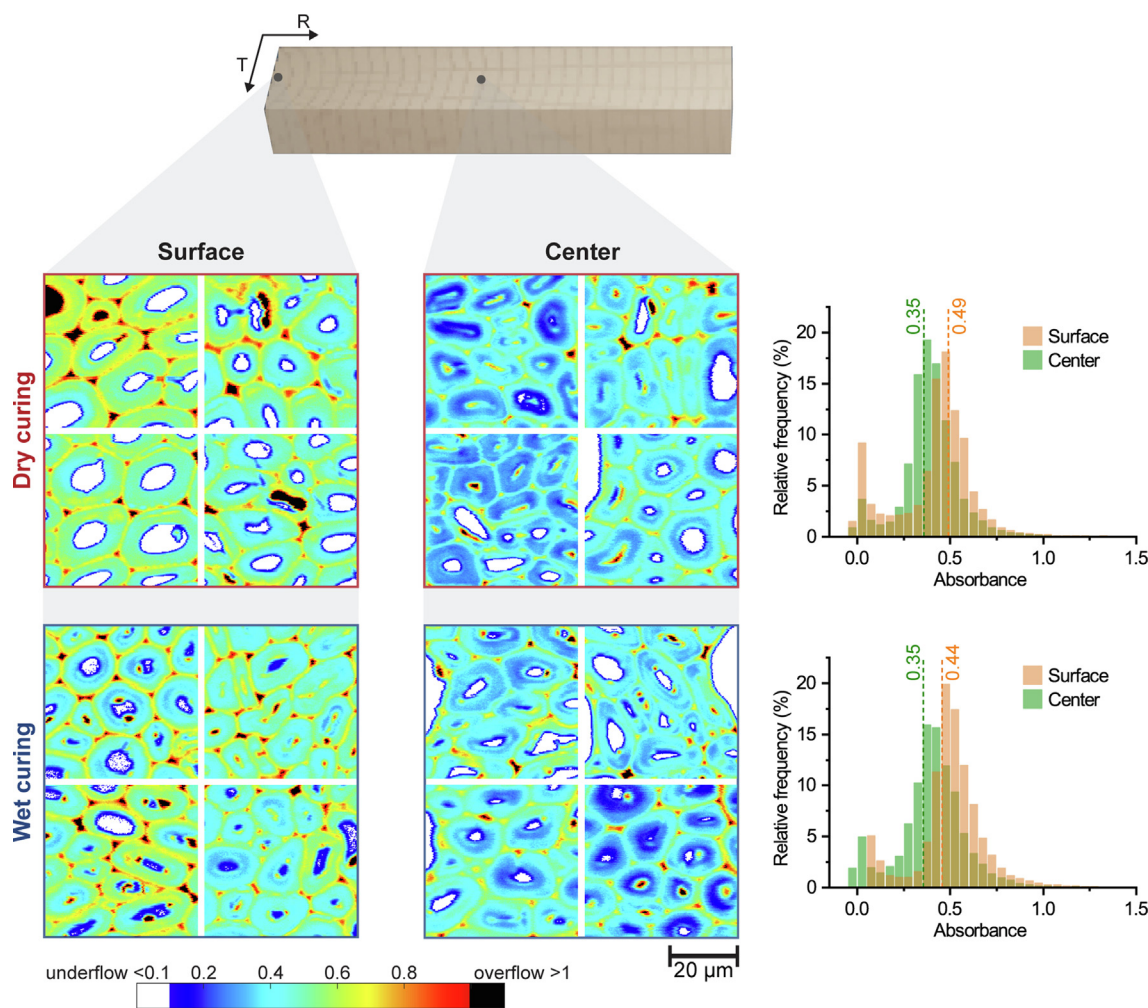


Fig. 9. Representative UMSP images taken from surface or center regions of board sections with sealed cross-sections during heat curing and pixel histograms based on all UMSP images per sample group ($n = 12$). The dashed lines highlight the average UV absorbance from ten selected regions within secondary cell walls.

Aalto University Bioeconomy Infrastructure. English-language proofreading was provided by Heidi Henrickson.

Appendix A. Supplementary material

Supplementary data to this article can be found online at <https://doi.org/10.1016/j.matdes.2022.111481>.

References

- [1] T. Belt, T. Keplinger, T. Hänninen, L. Rautkari, Cellular level distributions of Scots pine heartwood and knot heartwood extractives revealed by Raman spectroscopy imaging, *Ind. Crops Prod.* 108 (2017) 327–335, <https://doi.org/10.1016/j.indcrop.2017.06.056>.
- [2] M. Felhofer, B. Prats-Mateu, P. Bock, N. Gierlinger, Antifungal stilbene impregnation: transport and distribution on the micron-level, *Tree Physiol.* 38 (2018) 1526–1537, <https://doi.org/10.1093/treephys/tpy073>.
- [3] T. Belt, M. Venäläinen, M. Altgen, A. Harju, L. Rautkari, Extractive concentrations, and cellular-level distributions change radially from outer to inner heartwood in Scots pine, *Tree Physiol.* 41 (2021) 1034–1045, <https://doi.org/10.1093/treephys/tpaa166>.
- [4] T. Keplinger, F.K. Wittel, M. Rüggeberg, I. Burgert, Wood derived cellulose scaffolds—processing and mechanics, *Adv. Mater.* 33 (2021) 2001375, <https://doi.org/10.1002/adma.202001375>.
- [5] T. Keplinger, X. Wang, I. Burgert, Nanofibrillated cellulose composites and wood derived scaffolds for functional materials, *J. Mater. Chem. A* 7 (2019) 2981–2992, <https://doi.org/10.1039/C8TA10711D>.
- [6] C. Chen, Y. Kuang, S. Zhu, I. Burgert, T. Keplinger, A. Gong, T. Li, L. Berglund, S.J. Eichhorn, L. Hu, Structure–property–function relationships of natural and engineered wood, *Nat. Rev. Mater.* 5 (2020) 642–666, <https://doi.org/10.1038/s41578-020-0195-z>.
- [7] D.N.R. Smith, R. Cockcroft, A Method of obtaining uniform distribution of wood preservatives in toxicity test blocks, *Nature*. 189 (1961) 163–164, <https://doi.org/10.1038/189163a0>.
- [8] T.P. Schultz, D.D. Nicholas, T.J. Dalton, D. Keefe, Biocide retention variation of southern yellow pine products treated with waterborne preservatives in commercial, pilot plant, or laboratory cylinders, *For. Prod. J.* 54 (2004) 85–90.
- [9] A. Klüppel, C. Mai, The influence of curing conditions on the chemical distribution in wood modified with thermosetting resins, *Wood Sci. Technol.* 47 (2013) 643–658, <https://doi.org/10.1007/s00226-013-0530-2>.
- [10] K. Kurkowiak, A.K. Mayer, L. Emmerich, H. Militz, Investigations of the chemical distribution in sorbitol and citric acid (SorCA) treated wood—development of a quality control method on the basis of electromagnetic radiation, *Forests*. 13 (2022) 151, <https://doi.org/10.3390/f13020151>.
- [11] M.-S. Ilvessalo-Pfäffli, *Fiber Atlas - Identification of Papermaking Fibers*, Springer, Berlin Heidelberg, 1995.
- [12] A. Klüppel, Hardness and indentation modulus of resin-treated wood, *Int. Wood Prod. J.* 8 (2017) 41–44, <https://doi.org/10.1080/20426445.2016.1268358>.
- [13] V. Biziks, S. Bicke, G. Koch, H. Militz, Effect of phenol-formaldehyde (PF) resin oligomer size on the decay resistance of beech wood, *Holzforschung*. 75 (2021) 574–583, <https://doi.org/10.1515/hf-2020-0020>.
- [14] T. Furuno, Y. Imamura, H. Kajita, The modification of wood by treatment with low molecular weight phenol-formaldehyde resin: a properties enhancement with neutralized phenolic-resin and resin penetration into wood cell walls, *Wood Sci. Technol.* 37 (2004) 349–361, <https://doi.org/10.1007/s00226-003-0176-6>.
- [15] R.M. Seborg, H. Tarkow, A.J. Stamm, *Modified Woods*, Report No 2192 (revised), Forest Products Laboratory, Madison, WI, 1962.
- [16] A. Tarmian, I. Zahedi Tajrishi, R. Oladi, D. Efhamisizi, Treatability of wood for pressure treatment processes: a literature review, *Eur. J. Wood Wood Prod.* 78 (2020) 635–660, <https://doi.org/10.1007/s00107-020-01541-w>.

- [17] P. Zheng, D. Aoki, M. Seki, T. Miki, S. Tanaka, K. Kanayama, Y. Matsushita, K. Fukushima, Visualization of solute diffusion into cell walls in solution-impregnated wood under varying relative humidity using time-of-flight secondary ion mass spectrometry, *Sci. Rep.* 8 (2018) 9819, <https://doi.org/10.1038/s41598-018-28230-2>.
- [18] M. Altgen, M. Awais, D. Altgen, A. Klüppel, M. Mäkelä, L. Rautkari, Distribution and curing reactions of melamine formaldehyde resin in cells of impregnation-modified wood, *Sci. Rep.* 10 (2020) 3366, <https://doi.org/10.1038/s41598-020-60418-3>.
- [19] L. Emmerich, M. Bleckmann, S. Strobusch, C. Brischke, S. Bollmus, H. Militz, Growth behavior of wood-destroying fungi in chemically modified wood: wood degradation and translocation of nitrogen compounds, *Holzforschung*, 75 (2021) 786–797, <https://doi.org/10.1515/hf-2020-0252>.
- [20] A. Sangregorio, A. Muralidhara, N. Guigo, L.G. Thygesen, G. Marlair, C. Angelici, E. de Jong, N. Sbirrazzuoli, Humin based resin for wood modification and property improvement, *Green Chem.* 22 (2020) 2786–2798, <https://doi.org/10.1039/C9GC03620B>.
- [21] K.-C. Mahnert, S. Adamopoulos, G. Koch, H. Militz, Topochemistry of heat-treated and N-methylol melamine-modified wood of koto (*Pterygota macrocarpa* K. Schum.) and limba (*Terminalia superba* Engl. et. Diels), *Holzforschung*, 67 (2012) 137–146, <https://doi.org/10.1515/hf-2012-0017>.
- [22] T. Ma, T. Inagaki, M. Ban, S. Tsuchikawa, Rapid identification of wood species by near-infrared spatially resolved spectroscopy (NIR-SRS) based on hyperspectral imaging (HSI), *Holzforschung*, 73 (2019) 323–330, <https://doi.org/10.1515/hf-2018-0128>.
- [23] A. Thumm, M. Riddell, B. Nanayakkara, J. Harrington, R. Meder, Near infrared hyperspectral imaging applied to mapping chemical composition in wood samples, *J. Infrared Spectrosc.* 18 (2010) 507–515, <https://doi.org/10.1255/jnirs.909>.
- [24] H. Kobori, N. Gorretta, G. Rabatel, V. Bellon-Maurel, G. Chaix, J.-M. Roger, S. Tsuchikawa, Applicability of Vis-NIR hyperspectral imaging for monitoring wood moisture content (MC), *Holzforschung*, 67 (2013) 307–314, <https://doi.org/10.1515/hf-2012-0054>.
- [25] M. Awais, M. Altgen, M. Mäkelä, T. Belt, L. Rautkari, Quantitative prediction of moisture content distribution in acetylated wood using near-infrared hyperspectral imaging, *J. Mater. Sci.* 57 (2022) 3416–3429, <https://doi.org/10.1007/s10853-021-06812-2>.
- [26] P. Stefansson, I. Burud, T. Thiis, L. Gobakken, E. Larnøy, Estimation of phosphorus-based flame retardant in wood by hyperspectral imaging—a new method, *J. Spectr. Imag.* 7 (2018), <https://doi.org/10.1255/jsi.2018.a3.a3>.
- [27] M. Awais, M. Altgen, M. Mäkelä, D. Altgen, L. Rautkari, Hyperspectral near-infrared image assessment of surface-acetylated solid wood, *ACS Appl. Bio Mater.* 3 (2020) 5223–5232, <https://doi.org/10.1021/acsabm.0c00626>.
- [28] M. Mäkelä, M. Altgen, T. Belt, L. Rautkari, Hyperspectral imaging and chemometrics reveal wood acetylation on different spatial scales, *J. Mater. Sci.* 56 (2021) 5053–5066, <https://doi.org/10.1007/s10853-020-05597-0>.
- [29] EN84:2020, Durability of wood and wood-based products - Accelerated ageing of treated wood prior to biological testing - Leaching procedure, European Committee for Standardization, Brussels, Belgium.
- [30] Eigenvector Research Documentation Wiki, Box filter, 2019. <https://wiki.eigenvector.com/index.php?title=Box_filter> (Accessed February 24, 2022).
- [31] S. Wold, K. Esbensen, P. Geladi, Principal component analysis, *Proc. Multivar. Stat. Workshop Geol. Geochem.* 2 (1987) 37–52, [https://doi.org/10.1016/0169-7439\(87\)80084-9](https://doi.org/10.1016/0169-7439(87)80084-9).
- [32] M. Mäkelä, P. Geladi, M. Rissanen, L. Rautkari, O. Dahl, Hyperspectral near infrared image calibration and regression, *Anal. Chim. Acta.* 1105 (2020) 56–63, <https://doi.org/10.1016/j.aca.2020.01.019>.
- [33] Eigenvector Research Documentation Wiki, Svn, 2008. <<https://wiki.eigenvector.com/index.php?title=Svn>> (Accessed February 24, 2022).
- [34] M.E. Wall, A. Rechtsteiner, L.M. Rocha, Singular value decomposition and principal component analysis, in: D.P. Berrar, W. Dubitzky, M. Granzow (Eds.), *Pract. Approach Microarray Data Anal*, Springer, Boston, 2003.
- [35] P. Geladi, B.R. Kowalski, Partial least-squares regression: a tutorial, *Anal. Chim. Acta.* 185 (1986) 1–17, [https://doi.org/10.1016/0003-2670\(86\)80028-9](https://doi.org/10.1016/0003-2670(86)80028-9).
- [36] S. de Jong, SIMPLS: an alternative approach to partial least squares regression, *Chemom. Intell. Lab. Syst.* 18 (1993) 251–263, [https://doi.org/10.1016/0169-7439\(93\)85002-X](https://doi.org/10.1016/0169-7439(93)85002-X).
- [37] M. Andersson, A comparison of nine PLS1 algorithms, *J. Chemom.* 23 (2009) 518–529, <https://doi.org/10.1002/cem.1248>.
- [38] A.R. Spurr, A low-viscosity epoxy resin embedding medium for electron microscopy, *J. Ultrastruct. Res.* 26 (1969) 31–43, [https://doi.org/10.1016/S0022-5320\(69\)90033-1](https://doi.org/10.1016/S0022-5320(69)90033-1).
- [39] G. Kleist, U. Schmitt, Evidence of accessory compounds in vessel walls of Sapelli heartwood (*Entandrophragma cylindricum*) obtained by transmission electron microscopy, *Holz Als Roh-Werkst.* 57 (1999) 93–95, <https://doi.org/10.1007/PL00002633>.
- [40] K.B. Beć, J. Grabska, M.A. Czarnecki, Spectra-structure correlations in NIR region: spectroscopic and anharmonic DFT study of n-hexanol, cyclohexanol and phenol, *Festschr. Honor Prof. Yukihiko Ozaki*, 197 (2018) 176–184, <https://doi.org/10.1016/j.saa.2018.01.041>.
- [41] L. Dykes, L. Hoffmann, O. Portillo-Rodriguez, W.L. Rooney, L.W. Rooney, Prediction of total phenols, condensed tannins, and 3-deoxyanthocyanidins in sorghum grain using near-infrared (NIR) spectroscopy, *J. Cereal Sci.* 60 (2014) 138–142, <https://doi.org/10.1016/j.jcs.2014.02.002>.
- [42] C.N.T. Frizon, G.A. Oliveira, C.A. Perussello, P.G. Peralta-Zamora, A.M.O. Camlofski, Ü.B. Rossa, R. Hoffmann-Ribani, Determination of total phenolic compounds in yerba mate (*Ilex paraguariensis*) combining near infrared spectroscopy (NIR) and multivariate analysis, *LWT - Food Sci. Technol.* 60 (2015) 795–801, <https://doi.org/10.1016/j.lwt.2014.10.030>.
- [43] L. Ma, Y. Peng, Y. Pei, J. Zeng, H. Shen, J. Cao, Y. Qiao, Z. Wu, Systematic discovery about NIR spectral assignment from chemical structural property to natural chemical compounds, *Sci. Rep.* 9 (2019) 9503, <https://doi.org/10.1038/s41598-019-45945-y>.
- [44] M. Schwanninger, J.C. Rodrigues, K. Fackler, A review of band assignments in near infrared spectra of wood and wood components, *J. Near Infrared Spectrosc.* 19 (2011) 287–308, <https://doi.org/10.1255/jnirs.955>.
- [45] S. Tsuchikawa, Non-traditional applications of near infrared spectroscopy based on the optical characteristic models for a biological material having cellular structure, *J. Near Infrared Spectrosc.* 6 (1998) 41–46, <https://doi.org/10.1255/jnirs.119>.
- [46] M. Altgen, D. Altgen, A. Klüppel, L. Rautkari, Effect of curing conditions on the water vapor sorption behavior of melamine formaldehyde resin and resin-modified wood, *J. Mater. Sci.* 55 (2020) 11253–11266, <https://doi.org/10.1007/s10853-020-04814-0>.
- [47] Z. Li, X. Zhang, S. Song, K. Xu, J. Lyu, X. Li, Curing characteristics of low molecular weight melamine-urea-formaldehyde (MUF) resin-impregnated poplar wood, *Constr. Build. Mater.* 325 (2022), <https://doi.org/10.1016/j.conbuildmat.2022.126814> 126814.
- [48] G. Koch, G. Kleist, Application of scanning UV microspectrophotometry to localise lignins and phenolic extractives in plant cell walls 55 (2001) 563–567. doi: 10.1515/HF.2001.091.
- [49] Y. Musha, D.A.I. Goring, Distribution of syringyl and guaiacyl moieties in hardwoods as indicated by ultraviolet microscopy, *Wood Sci. Technol.* 9 (1975) 45–58, <https://doi.org/10.1007/BF00351914>.
- [50] J.S. Kim, Y.Y. Lee, T.H. Kim, A review on alkaline pretreatment technology for bioconversion of lignocellulosic biomass, *Bioresour. Technol.* 199 (2016) 42–48, <https://doi.org/10.1016/j.biortech.2015.08.085>.
- [51] J.F. Siau, *Transport Processes in Wood*, Springer Science & Business Media, 2012.
- [52] M. Sedighi-Gilani, P. Vontobel, E. Lehmann, J. Carmeliet, D. Derome, Liquid uptake in Scots pine sapwood and hardwood visualized and quantified by neutron radiography, *Mater. Struct.* 47 (2014) 1083–1096, <https://doi.org/10.1617/s11527-013-0112-7>.
- [53] A. Bastani, S. Adamopoulos, H. Militz, Water uptake and wetting behaviour of furfurylated, N-methylol melamine modified and heat-treated wood, *Eur. J. Wood Wood Prod.* 73 (2015) 627–634, <https://doi.org/10.1007/s00107-015-0919-8>.